CELLULAR VORTEX FORMATION BETWEEN A HEATED HORIZONTAL CYLINDER AND AN ADIABATIC UPPER WALL

Marc-Etienne Lamarche-Gagnon
National Research Council of Canada
75 de Mortagne Boulevard, Boucherville, Quebec J4B 6Y4, Canada
marc-etienne.lamarche-gagnon@nrc-cnrc.gc.ca

Stavros Tavoularis
Department of Mechanical Engineering, University of Ottawa
161 Louis Pasteur, Ottawa, Ontario K1N 6N5, Canada
stavros.tavoularis@uottawa.ca

ABSTRACT

Experimental studies of laminar flow instability between a heated horizontal cylinder and an adiabatic ceiling have identified the formation of axially periodic convection patterns in the gap region for gap-to-cylinder-diameter ratios $0.1 \leq h/d \leq 0.5$ and Rayleigh numbers $Ra \gtrsim 2 \times 10^6$. Computations for a uniformly heated cylinder wall and for $h/d = 0.2$ show that, in the range $3 \times 10^6 \lesssim Ra \lesssim 5 \times 10^6$, two pairs of steady roller-type vortices appeared in the gap region, whereas, for $Ra \gtrsim 1 \times 10^7$, the rollers broke down to quasi-steady, axially periodic, toroidal convection cells.

INTRODUCTION

Natural convection, namely fluid motion produced by density differences in non-isothermal flows, has attracted intense attention, due to its intrinsic scientific interest as well as its occurrence in a multitude of environmental and technological systems. The onset of various flow instabilities and the resulting patterns of fluid motion in natural convection have customarily been correlated with the value of the Rayleigh number, which may be viewed as the ratio of the time scales for heat diffusion and heat convection. Of particular interest has been the cellular structure that is the result of flow instability in such systems under certain conditions. The case that has received the most detailed documentation is Rayleigh-Bénard convection, which refers to flow patterns forming in the space between two horizontal plane surfaces, maintained at constant temperatures and the lower of which has a higher temperature than the upper one (Bodenschatz *et al.*, 2000; Lohse & Xia, 2010). One may anticipate that cellular convection may occur under certain conditions in systems with different geometries, but systematic studies of such phenomena are rather scarce. A case that has attracted some attention is natural convection from a heated cylinder at different orientations in the vicinity of different boundaries. Such investigations have been mainly conducted for two idealised types of boundary conditions for the cylinder wall: a uniform temperature (*Dirichlet condition*) or a uniform heat flux (*Neumann condition*); a third, mixed, type of boundary condition (*Robin condition*) has also been used in analytical studies to describe more realistically conditions in physical systems.

The present interest is focused on natural convection above a horizontal heated cylinder with a diameter d in a fluid that is bounded from above by an adiabatic horizontal ceiling, located at a distance h above the cylinder. This is an idealisation of configurations found in heat exchangers, suspended pipes carrying a hot fluid and electronic devices. For a horizontal cylinder with a uniform surface temperature T_c, the Rayleigh number is defined as

$$Ra = \frac{g\beta d^3 \Delta T_c}{\nu\alpha},\qquad(1)$$

where g is the gravitational acceleration, $\beta \approx 1/T_f$ is the thermal expansion coefficient of the fluid, $T_f = (T_c + T_a)/2$ is the film temperature, T_a is the far-field (ambient) temperature, $\Delta T_c = T_c - T_a$, and ν, α are, respectively, the kinematic viscosity and the thermal diffusivity of the fluid, both evaluated at the film temperature. For cases with a uniform cylinder-wall heat flux $\dot{q}$, the usual version of this parameter is the modified Rayleigh number

$$Ra^* = \frac{g\beta d^4 \dot{q}}{k\nu\alpha},\qquad(2)$$

where k is the thermal conductivity of the fluid at film temperature.

For relatively large h/d, one would expect that a buoyant plume would rise above the cylinder and behave like an unconfined plume, which is unstable for sufficiently large Ra. For small h/d, one may anticipate that the convection pattern would, besides h/d, depend on the thermal states of both the cylinder and the ceiling. Studies with a non-adiabatic ceiling (Atmane *et al.*, 2003; Koizumi & Hosokawa, 1996; Kumar *et al.*, 2014) found that, when h was larger than a few d, the rising thermal plumes developed quasi-periodic, swaying motions for a wide range of Ra, but, when h was reduced below d, flow unsteadiness appeared in the form of a chaotic motion. Studies with an adiabatic ceiling are relatively few and extended over limited ranges of conditions. In an experimental study of a cylinder with a uniform surface temperature inside an air-filled vessel with an adiabatic ceiling, Koizumi & Hosokawa (1996) observed the formation of thermal plumes, which they found to be stable under all examined conditions ($4.8 \times 10^4 \leq Ra \leq 1 \times 10^7$ and $0.05 \leq h/d \leq 2.3$).

In a similar experimental study, but with the vessel open on both sides, Ashjaee *et al.* (2007) found that two-dimensional vortices formed in the gap region for $Ra = 1.5 \times 10^4$ and $h/d < 0.5$. Vortices in the gap region were also found to form in a two-dimensional numerical study by Ashjaee *et al.* (2014). In summary, the literature shows no evidence for the formation of cellular patterns, or any other form of flow instability, between a heated cylinder and an adiabatic ceiling. The objective of the present work is to examine, both experimentally and computationally, whether there are conditions under which the two-dimensional vortices that have been observed to form in the cylinder-ceiling gap would break down and, when this happens, whether they would be replaced by three-dimensional cells or any other type of structures.

EXPERIMENTAL METHODOLOGY

The experimental apparatus is shown schematically in Fig. 1. A schedule 40 cylindrical tube, made of polyvinyl chloride (PVC) and having an outer diameter $d = 168\,\text{mm} \pm 0.5\,\%$ and a length $l = 6.05\,\text{m}$, was suspended horizontally below a horizontal ceiling, made of polystyrene foam, $w = 1.22\,\text{m}$ wide and 50.8 mm thick. Sagging due to the cylinder weight was reduced by fitting it with a coaxial aluminium pipe and by resting it on two vertically adjustable pins, each located at a distance $l/3$ from the corresponding end, so that the central third of the cylinder was unobstructed by these pins. The remaining sag in the cylinder middle region did not exceed 1 mm ($= 0.006d$). Each cylinder end was mounted on a custom-made, precision vertical traversing system, so that its distance h from the ceiling could be adjusted to the desired value, within the range $0 \lesssim h/d \lesssim 5$. Vertical panels, made of the same material as the ceiling, were attached to the two ends of the cylinder to insulate the test section from the surrounding room. The cylinder was wrapped with a 0.05 mm thick stainless steel foil, which was painted flat black and was heated electrically with the use of a high-current/low-voltage power supply.
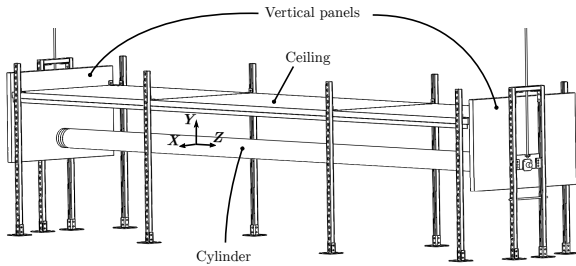

Figure 1: The experimental facility.

The temperature at selected points on the cylinder surface was measured with flush-mounted thermistors and RTD elements. Two fast-response thermistors, mounted on a triaxial traversing mechanism, were used to measure the local air temperature in the gap region. The surface temperature of the ceiling bottom was measured with an infrared camera (FLIR A325sc), having 320×240 pixels and equipped with a 45° field-of-view lens. Optical distortions caused by the camera inclination were corrected analytically. The surface-averaged convective heat transfer coefficient from the cylinder was calculated from the supplied electric power after subtracting cable power losses and radiation heat transfer estimates.

COMPUTATIONAL METHODOLOGY

The computational domain, shown in Fig. 2, was meant to approximate the experimental setup. The domain dimensions, normalised by the cylinder diameter, were $D = 1$, $L = 10$,

$W_d = 9$, and $H_d = 2.5$. The normalised distance H between the cylinder and the ceiling was in the range $0.1 \le H \le 1.0$.
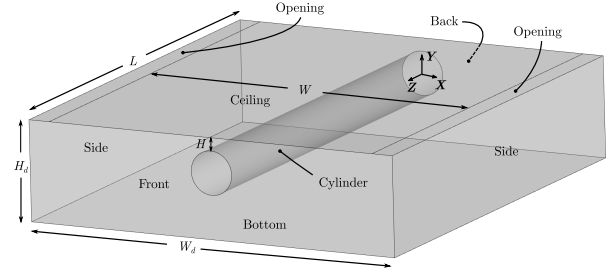

Figure 2: The computational domain.

The simulations were performed with the open source finite volume code OpenFOAM V7 (https://www.openfoam.com/). The `buoyantPimpleFoam` solver and the PISO algorithm were employed to solve the continuity, momentum and energy equations for slightly compressible laminar flow. Numerical schemes were all of second order, implicit in time and centred in space, except for the energy equation for which an adaptive upwind scheme was used. The time step was chosen so that the Courant number was everywhere less than 1, and further by ensuring that the time step was at least one or two orders of magnitude smaller than the period of any existing fluctuations. The solution was found to be insensitive to a reduction of the Courant number to 0.2.

No-penetration and no-slip conditions were applied to the cylinder and the front and back domain boundaries. The inlet-outlet condition, which consists of a Neumann condition for outward flows and a Dirichlet condition for inward flows, was applied to the sides to account for possible flow reversal, which was indeed observed in some cases. The main boundary from which the flow was allowed to enter the domain was from the bottom, where a "pressure inlet" condition was used. The upper boundary was divided into a solid central section and two open narrow sections, from which fluid could exit the domain. The "fixed-flux-pressure" condition was used for the cylinder, the solid ceiling and the front and back boundaries. For the bottom and sides, the total alternative pressure was set to $p' = p_a + 0.5\rho \|\boldsymbol{u}\|^2$, where $p_a = 10^5$ Pa, approximately equal to the standard atmospheric pressure. A zero-gradient condition was imposed on the openings. The temperature on the sides and the bottom was fixed at $T_a = 300$ K, whereas the ceiling, front, back and opening boundaries were made adiabatic. Computations were performed with three types of thermal conditions on the cylinder surface: constant temperature, constant heat flux and a mixed type (Robin condition). The fluid was air, modelled as an ideal gas with viscosity and thermal conductivity, evaluated using the Sutherland approximation.

Validation was done by comparing the computed, surface-averaged, Nusselt number at different *Ra* with the prediction of the Churchill & Chu (1975) correlation for natural convection from an unconfined, horizontal cylinder.

PRELIMINARY COMPUTATIONS

In the absence of guidance from the literature concerning conditions for possible flow instability, and to avoid time-consuming parametric experimental and 3-D computational studies, we performed exploratory 2-D simulations. Our interest was focussed on laminar flows and we speculated that, in the present configuration, the upper limit of Rayleigh number for laminar flow would be comparable, in order-of-magnitude, to the one for natural convection from unconfined, heated, horizontal cylinders, which is roughly 1×10^9, for a uniform

(a) $H = 0.1$, $Ra = 6.62 \times 10^6$ (b) $H = 0.2$, $Ra = 6.62 \times 10^6$

(c) $H = 0.2$, $Ra = 1.23 \times 10^7$ (d) $H = 0.3$, $Ra = 1.23 \times 10^7$

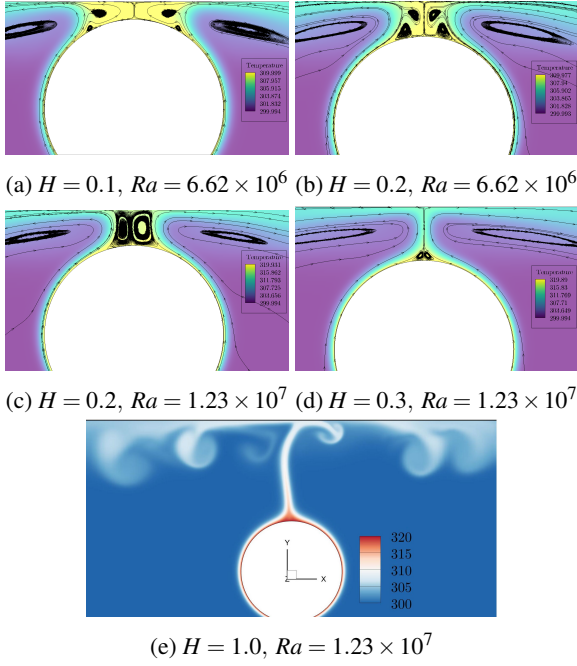(e) $H = 1.0$, $Ra = 1.23 \times 10^7$

Figure 3: Instantaneous streamlines and temperature flood maps, obtained by two-dimensional computations with a uniform cylinder temperature.

temperature cylinder (Churchill & Chu, 1975), and 2×10^9, for a uniform wall heat flux cylinder (Kitamura *et al.*, 1999). First, we imposed a uniform temperature on the cylinder surface (see Figure 3 for representative results). We observed that large, stable 2D vortices were generated for $H = 0.1$ and $H = 0.2$ and $Ra \gtrsim 6.62 \times 10^6$, whereas for $H = 0.3$ and $H = 0.5$ only small separation bubbles attached to the cylinder surface were formed. For $H = 1.0$, the plume became unstable, as it impacted on the ceiling. Next, we imposed a uniform wall heat flux (*i.e.*, a uniform temperature gradient) on the cylinder surface. Vortices were only noticed for $H = 0.1$ and $Ra^* \gtrsim 2 \times 10^8$. In summary, the 2-D simulations showed that vortical structures in the gap region were only generated for $H = 0.1$ and 0.2 and for sufficiently large Rayleigh numbers. These structures were always found to be stable, which excludes the presence of any 2-D instability mechanism.

We also performed a number of exploratory 3-D simulations. When a uniform heat flux was applied, all 3-D results were nearly identical to the 2-D ones. The flow did not show any evidence of axial motions and the vortices in the gap region, whenever they appeared, remained 2-D and stable. When a uniform temperature was applied on the cylinder, the 3-D results were also the same as the 2-D results for configurations having $H = 0.1$, 0.3 and 0.5. In sharp contrast, however, the 2-D vortices became unstable and broke down to toroidal ones for the configuration having $H = 0.2$ when $Ra \gtrsim 7 \times 10^6$.

EXPERIMENTAL RESULTS

All measurements were collected under quasi-steady conditions, typically achieved five hours after powering the foil. Measurements were collected for $H = 0.1$, 0.2, 0.5 and 1.0 and various heating powers, as listed in Table 1.

The cylinder surface temperature rise ΔT_c varied between a minimum at the bottom of the cylinder and a maximum at the top, so the experiments are clearly not under constant wall temperature conditions. The measured azimuthal wall temperature profile was found to be substantially less non-uniform

Case	H	$\Delta T_{c,av}$	$\dot{q}_{c,av}$	Ra_{av}	Ra^*_{av}
	–	[K]	[W m^{-2}]	–	–
a	0.1	2.2	2.7	1.0×10^6	7.7×10^6
b	0.1	4.2	7.1	1.9×10^6	2.0×10^7
c	0.2	5.0	2.4	2.2×10^6	6.7×10^6
d	0.2	16.0	57.1	6.6×10^6	1.5×10^8
e	0.5	3.4	11.2	1.5×10^6	3.2×10^7
f	0.5	16.0	69.1	6.6×10^6	1.8×10^8
g	1	15.9	69.4	6.5×10^6	1.8×10^8

Table 1: Experimental conditions, averaged over the cylinder surface.

than the one obtained computationally for a constant heat flux, but matched fairly well the profile obtained computationally using a tuned Robin condition (see Figure 4). The moderation of the non-uniformity of the measured wall temperature profile is attributed largely to heat conduction within the cylinder.
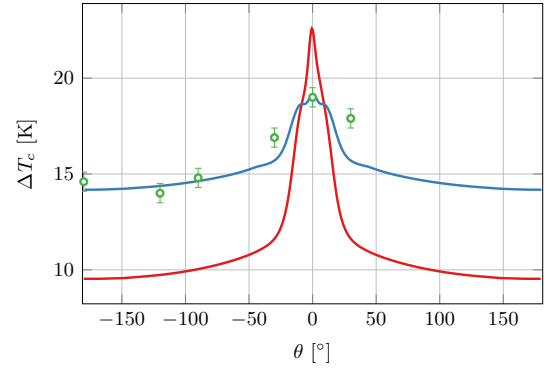

Figure 4: Azimuthal profiles of measured cylinder surface temperature rise for Case d (symbols and uncertainty bars), along with profiles extracted from simulations using a uniform wall heat flux (red line) or the Robin condition (blue line).

The experimental results revealed the presence of quasi-spatially-periodic and weakly unsteady convection cells in the gap region between the cylinder and the ceiling for $0.1 \leq H \leq 0.5$ and $Ra \gtrsim 2 \times 10^6$. These cells comprised alternating (axially) regions with higher and lower temperature, as demonstrated by their signatures on instantaneous contour maps of the ceiling temperature, obtained with the infrared camera. Representative examples of such contour maps and corresponding axial profiles of temperature for Case d ($H = 0.2$, $Ra_{av} = 6.6 \times 10^6$) are shown in Figure 5. The measurable transverse (namely, in the X direction) extent of the convection cells was comparable to the cylinder diameter. Each cell occasionally shifted axially or merged with an adjacent cell to form a larger one. The typical lifetime of each cell was between a few seconds and a few tens of seconds.

The statistical distribution of the axial spacing between cells was determined from a large number of axial wavenumber spectra of temperature at different instances. For each temperature map, spectra were computed on lines of constant X, for all 20 transverse X pixels of the corresponding image, and then averaged together. Each averaged spectrum was then visually inspected in its pre-multiplied form to evaluate the most energetic and second most energetic wavenumbers, namely, the ones showing the largest and the second largest peak. The resulting probability density functions (pdf) of the two peaks
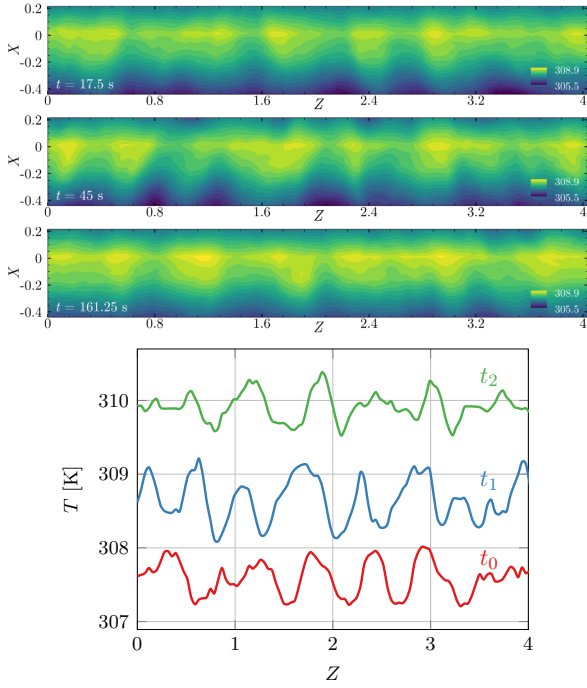
Figure 5: Top: three sets of instantaneous iso-contour maps of the ceiling temperature, obtained with the infrared camera for Case d; contour levels are separated by 0.2 K. Bottom: axial profiles of the ceiling temperature at $X = -0.24$ at the same instants as those in the maps (profiles for the two later instants are offset by 1 K and 2 K, respectively, to avoid clutter).
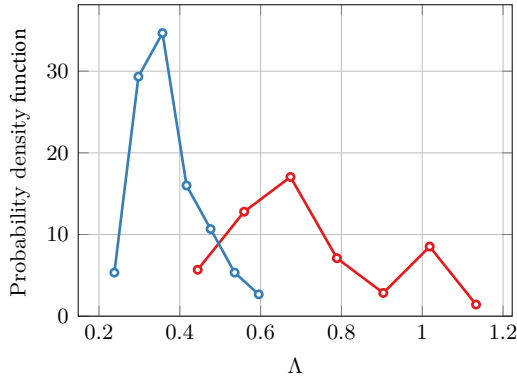

Figure 6: Probability density function of the most energetic (red line) and second most energetic (blue line) wavelengths for case d.

of the dimensionless wavelength $\Lambda = \lambda/d$ are shown in Figure 6. The pdf of the most energetic wavelength shows a bimodal distribution, with peaks at $\Lambda \approx 0.65$ and $\Lambda \approx 1$. The lower wavelength is the dominant spacing between distinct cells, whereas the higher one can be attributed to the presence of merging cells. The pdf of the second most energetic wavelength is unimodal, with a peak at $\Lambda \approx 0.33$, *i.e.*, about half of the most energetic wavelength; it is attributed to cell breakdown.

To investigate the nature of flow unsteadiness, frequency spectra $E_T(f)$ of the ceiling temperature time series at various (Z, X) positions were computed and spatially averaged over the image domain. The resulting pre-multiplied spectrum is shown in Figure 7. One can observe that the most energetic frequencies lied in the band $0.01\,\text{Hz} \lesssim f \lesssim 0.05\,\text{Hz}$, which is
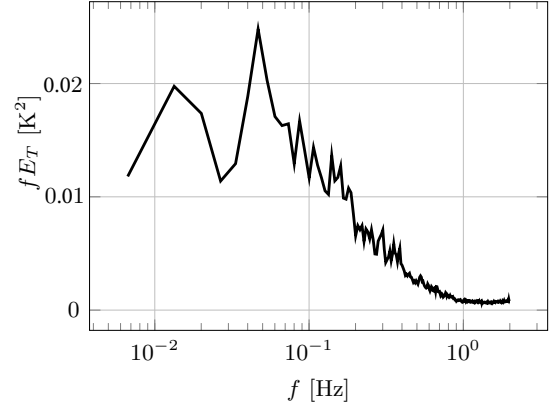

Figure 7: Pre-multiplied, spacially averaged, frequency spectrum of the ceiling temperature for case d.

consistent with the presence of low-frequency modulations observed in the time series. In addition, a considerable amount of energy was contained in the range 0.1–0.2 Hz.

In Case c, which had $H = 0.2$, like Case d, but the lower $Ra_{av} = 2.2 \times 10^6$, the cells were not as well defined and appeared in fewer than 50% of the images. The dominant wavelength was $\Lambda = 0.85$, thus, somewhat larger than that in Case d, and the transverse width of the cells was significantly larger. In cases with $H = 0.1$ and 0.5, no cellular patterns were observed at relatively small Rayleigh numbers (Case a, having $H = 0.1$ and $Ra_{av} = 1.0 \times 10^6$; Case e, having $H = 0.5$ and $Ra_{av} = 1.5 \times 10^6$), but they were observable at higher Rayleigh numbers (Case b, having $H = 0.1$ and $Ra_{av} = 1.9 \times 10^6$; Case f, having $H = 0.5$ and $Ra_{av} = 6.6 \times 10^6$). As in Case c, however, cellular structures in cases b and f formed less frequently and were both wider and longer and had a shorter lifetime than those in Case d. For $H = 1$, we could not corroborate the formation of cellular patterns. For $Ra_{av} = 6.5 \times 10^6$ (Case g), higher temperature spots were observed on the ceiling but only for about 20 % of the time and oscillated across the symmetry plane. In view of the preliminary simulation results shown in Figure 3e and previous observations (Lin *et al.*, 2017), we may interpret these patterns as the signature of plume swaying motions.

In summary, for $H = 0.1$, 0.2 and 0.5, cellular patterns were observed experimentally for $Ra_{av} \gtrsim 2 \times 10^6$, but they were best defined for $H = 0.2$. The strength, size and lifetime of the cells depended upon H.

COMPUTATIONAL RESULTS

Guided by our preliminary simulations and experimental findings, we conducted extensive 3-D simulations only for the $H = 0.2$ geometry and for four different values of ΔT_c, *i.e.*, the difference between the uniform cylinder temperature and the far-field temperature, as listed in Table 2. All simulations started by imposing $\Delta T_c = 1$ K (Case A – $Ra = 7.08 \times 10^5$). Well after the solution converged, we suddenly imposed $\Delta T_c = 5$ K (Case B – $Ra = 3.43 \times 10^6$). After this solution converged, we imposed $\Delta T_c = 12$ K (Case C – $Ra = 7.82 \times 10^6$). Finally, once Case C reached an asymptotic state, we imposed $\Delta T_c = 20$ K (Case D – $Ra = 1.23 \times 10^7$), but we also examined a case in which we imposed $\Delta T_c = 20$ K directly after Case A converged. As in all our cases Ra was at least two orders of magnitude smaller than the transition Ra in natural convection from unconfined heated cylinders, we are confident that the flow would remain laminar throughout.

4

Case	H	ΔT_c [K]	Ra
A	0.2	1	7.08×10^5
B	0.2	5	3.43×10^6
C	0.2	12	7.82×10^6
D	0.2	20	1.23×10^7

Table 2: Conditions of the main 3-D simulations.

For $Ra = 7.1 \times 10^5$, the flow above the cylinder was steady and no vortices were formed. For $Ra = 3.4 \times 10^6$, two pairs of steady counter-rotating roll vortices were identified by the Q-criterion (Figure 8, top). After Ra was raised to 7.8×10^6, each of the four rollers started to oscillate transversely with a normalised wavelength of about 0.24 and occasionally developed branches that approached an adjacent roller, eventually reaching a new quasi-steady state (Figure 8, bottom).
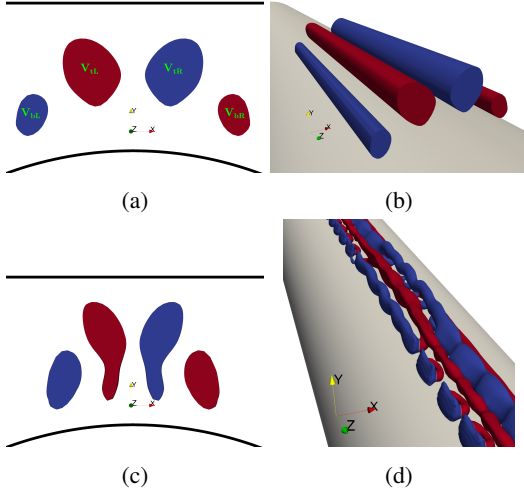

(a)   (b)

(c)   (d)

Figure 8: Cross-sections and 3-D views of the four main roller vortices, identified as $Q = 0.2$ s^{-2} isosurfaces, during the asymptotic states of Case B (top) and Case C (bottom); red indicates a positive axial vorticity component and blue a negative one.

For $Ra = 1.2 \times 10^7$, the vortex pattern was drastically different: it consisted of a series of well defined, toroidal vortex rings, that were nearly equally spaced along the cylinder axis and had a roughly rectangular axis shape (Figure 9). The dimensionless axial cell spacing ranged from 0.24 to 0.42 with an average of 0.35. Each toroidal vortex was linked at its top, on each side of the symmetry plane, with the two adjacent toroidal vortices.

The vortex cells appeared to be fairly stable and nearly spatially periodic most of the time. However, individual cells occasionally, though rather infrequently, became deformed and even broke down, thus, temporarily acquiring irregular shapes and uneven axial spacing; such events did not affect noticeably the average cell spacing. An example of an irregular cell can be observed in Figure 10a, in the range $5.0 \lesssim Z \lesssim 6.3$. A steady solution was never reached for $Ra \geq 7.82 \times 10^6$. As evidenced in Figure 9d by the direction of velocity vectors on Q-isosurfaces, warmer fluid from the near-cylinder region was moved upwards outside the cell, whereas cooler fluid from the ceiling region was moved downwards towards the inner base of the cell and tended to impinge on the cylinder wall. As a result, and, as Figure 10b shows, the local Nusselt number on the cylinder wall was significantly larger under cell interiors
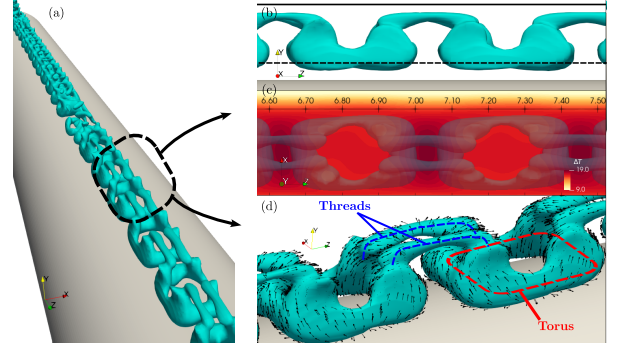

Figure 9: $Q = 1.2$ s^{-2} isosurfaces for Case D; a) three-dimensional view; b) detail side view; c) detail top view, along with a temperature rise flood map on the XZ plane indicated by the dashed line in b); d) three-dimensional detail, also showing velocity vectors on these surfaces.

than under inter-cellular spaces, with the ratio of these numbers along the symmetry plane reaching values near 2. Consequently, the temperature under the interior of the cells was lower than under inter-cellular regions, as can be seen in Figure 9c. Figure 10b also shows that convective heat transfer was augmented significantly (up to more than four times) under a broken cell (e.g., for $Z \approx 5.52$), which may be attributed to the additional mixing caused by cell breakdown. When, however, one considers heat transfer from the entire cylinder surface, as illustrated typically in Figure 10c, it is evident that, irrespectively of the cell location, heat transfer from the cylinder wall was much weaker in the gap region ($|\theta| \lesssim 15°$) than elsewhere. The maximum Nusselt number, which occurred on the bottom of the cylinder ($\theta = \pm 180°$), was an order of magnitude larger than levels in the gap region. It is also evident that fluctuations in the local cylinder Nusselt number, induced by the vortex cells, were restricted to the gap region.
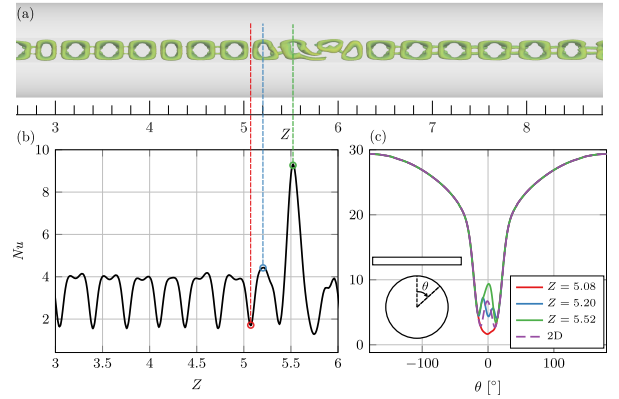

Figure 10: a) Instantaneous bottom view of $Q = 1.2$ s^{-2} isosurfaces in the gap region; b) axial profiles of the local cylinder Nusselt number along the $\theta = 0$ line at the same instant as the shown isosurfaces; c) circumferential profiles of the local cylinder Nusselt number at three axial positions and at the same instant as the presently shown isosurfaces, along with the profile obtained from the corresponding 2D computation.

DISCUSSION

The presently observed mechanism of cellular vortex formation resembles vortex pair instability mechanisms in different configurations (Kida & Takaoka, 1994; Hussain & Du-

5

raisamy, 2011; Yao & Hussain, 2022; Leweke *et al.*, 2016). Of particular interest has been the long-wave Crow instability (Crow, 1970), in which self- and mutual induction by the vortices cause an exponential growth of a disturbance and lead to the formation of three-dimensional vortex rings. Another case of interest is the short-wave elliptic instability (Kerswell, 2002), characterised by the development of perturbations within the core of each vortex. Despite the striking visual resemblance of the present toroidal cells with experimentally (Leweke & Williamson, 2011) and numerically (Laporte & Corjon, 2000) identified structures generated by Crow instability, there are essential differences in the nature of these two types of structures. In the present study, the structures are maintained by a continuous supply of buoyancy-generated kinetic energy and are confined ("trapped") in the gap region. As a result, they do not decay with time and are nearly fixed in space, in contrast to Crow-type vortices, both found in the far wake of aircraft or generated in the laboratory (Leweke & Williamson, 2011), which decay, as they get diffused. The stability thresholds of the two types of vortices are also very different: the circulation Reynolds number of the present vortices at the onset of instability is at least one to two orders of magnitude lower than those in other vortex breakdown cases. On the other hand, the average wavelength of the present toroidal structures, when normalised by the separation distance of the V_b and V_t vortices in each pair, prior to the start of the instability ($t \approx 20$ s, Case C, *cf.* Figure 8c), is equal to 4.7 and 5.8 in the asymptotic states of Case C and Case D, respectively. These values are comparable to values for the Crow instability, which range from 5 to 10 for an equal-strength vortex pair, but can be as low as 1 for vortex pairs with unequal strengths (Leweke *et al.*, 2016). Furthermore, the asymptotic state of Case C resembles the unequal-strength Crow instability vortices observed during an early stage in the experiments of Ortega *et al.* (2003) and in the computations of Chatelain *et al.* (2008) (see also Leweke *et al.* (2016)). Hence, although the toroidal cells in the present study cannot be classified as conventional Crow instability structures, the configuration and generation mechanisms of the two phenomena share some evident resemblances. One may finally note that the fact that the instability occurs for a very narrow range of conditions (especially the range of *H*) may explain why the presently found instability has never been reported in the literature.

CONCLUSIONS

The following main conclusions were based on both experimental and computational studies of natural convection in the gap region between a heated cylinder and an adiabatic ceiling.

1. A three-dimensional, buoyancy-induced instability was triggered when the gap-to-diameter ratio was within a range of small values and the Rayleigh number exceeded a threshold, causing the formation of cellular structures in the gap region.
2. The axial wavelength of these structures was comparable to half the cylinder diameter.
3. These structures occasionally shifted axially, broke down and merged with neighbouring ones.

ACKNOWLEDGEMENT

REFERENCES

Ashjaee, M, Bigham, S & Yazdani, S 2014 A numerical study on natural convention heat transfer from a horizontal isothermal cylinder located underneath an adiabatic ceiling. *Heat Transfer Eng* **35** (10), 953–962.

Ashjaee, M, Eshtiaghi, A H, Yaghoubi, M & Yousefi, T 2007 Experimental investigation on free convection from a horizontal cylinder beneath an adiabatic ceiling. *Exp Therm Fluid Sci* **32** (2), 614–623.

Atmane, M A, Chan, V SS & Murray, D B 2003 Natural convection around a horizontal heated cylinder: the effects of vertical confinement. *Int J Heat Mass Transf* **46** (19), 3661–3672.

Bodenschatz, E, Pesch, W & Ahlers, G 2000 Recent developments in Rayleigh–Bénard convection. *Annu Rev Fluid Mech* **32**, 709–788.

Chatelain, P, Curioni, A, Bergdorf, M, Rossinelli, D, Andreoni, W & Koumoutsakos, P 2008 Billion vortex particle direct numerical simulations of aircraft wakes. *Comput Methods Appl Mech Eng* **197** (13-16), 1296–1304.

Churchill, S W & Chu, H H S 1975 Correlating equations for laminar and turbulent free convection from a vertical plate. *Int J Heat Mass Trans* **18** (11), 1323–1329.

Crow, S C 1970 Stability theory for a pair of trailing vortices. *AIAA J* **8** (12), 2172–2179.

Hussain, F & Duraisamy, K 2011 Mechanics of viscous vortex reconnection. *Phys. Fluids* **23** (2), 021701.

Kerswell, R R 2002 Elliptical instability. *Annu Rev Fluid Mech* **34** (1), 83–113.

Kida, S & Takaoka, M 1994 Vortex reconnection. *Annu Rev Fluid Mech* **26** (1), 169–177.

Kitamura, K, Kami-Iwa, F & Misumi, T 1999 Heat transfer and fluid flow of natural convection around large horizontal cylinders. *Int J Heat Mass Transf* **42** (22), 4093–4106.

Koizumi, H & Hosokawa, I 1996 Chaotic behavior and heat transfer performance of the natural convection around a hot horizontal cylinder affected by a flat ceiling. *Int J Heat Mass Transf* **39** (5), 1081–1091.

Kumar, A, Joshi, J B, Nayak, A K & Vijayan, P K 2014 3d cfd simulation of air cooled condenser-i: Natural convection over a circular cylinder. *Int J Heat Mass Transf* **78**, 1265–1283.

Laporte, F & Corjon, A 2000 Direct numerical simulations of the elliptic instability of a vortex pair. *Phys. Fluids* **12** (5), 1016–1031.

Leweke, T, Le Dizes, S & Williamson, C HK 2016 Dynamics and instabilities of vortex pairs. *Annu Rev Fluid Mech* **48**, 507–541.

Leweke, T & Williamson, C HK 2011 Experiments on long-wavelength instability and reconnection of a vortex pair. *Phys Fluids* **23** (2), 024101.

Lin, K C, Bhosale, Y & Huang, C-Y Z 2017 3d-cfd investigation into free convection flow above a heated horizontal cylinder: Comparisons with experimental data. *Appl Therm Eng* **120**, 277–288.

Lohse, D & Xia, K-Q 2010 Small–scale properties of turbulent Rayleigh–Bénard convection. *Annu Rev Fluid Mech* **42**, 335–364.

Ortega, J M, Bristol, R L & Savaş, Ö 2003 Experimental study of the instability of unequal-strength counter-rotating vortex pairs. *J. Fluid Mech* **474**, 35–84.

Yao, J & Hussain, F 2022 Vortex reconnection and turbulence cascade. *Annu Rev Fluid Mech* **54**, 317–347.